Available online at www.sciencedirect.com
ScienceDirect
International Journal of Hydrogen Energy 32 (2007) 832–841
International Journal of HYDROGEN ENERGY
www.elsevier.com/locate/ijhydene

A two-phase model of an intermediate temperature PEM fuel cell

Denver F. Cheddie*, Norman D.H. Munroe

Mechanical and Materials Engineering, CEAS 2103, Florida International University, 10555 W Flagler Street, Miami, FL 33174, USA

Received 16 March 2006; received in revised form 18 October 2006; accepted 25 October 2006
Available online 12 December 2006

Abstract

A two-phase model of an intermediate temperature (120–200 °C) proton exchange membrane (PEM) fuel cell is presented. This model is an improvement on our previous intermediate temperature models, in that it accounts for two phase effects due to gas solubility in the phosphoric acid/polybenzimidazole (PBI) electrolyte, and considers aqueous phase electrochemical reactions. The model accounts for all polarization and transport phenomena, and exhibits a good fit with experimental data in the temperature range (150–170 °C). Parametric results are also presented, to investigate the dependence of the fuel cell performance on membrane doping level, catalyst activity, and transport properties of dissolved gases in the electrolyte medium. Results indicate that significant transport limitations exist at both electrodes, where catalyst utilization is between 0.1% and 1%. Alternative doping agents to phosphoric acid are suggested, as well as the need for more advanced catalyst deposition techniques.

Keywords: Two phase; PBI; Polybenzimidazole; PEM fuel cell modeling

1. Introduction

Proton exchange membrane fuel cells (PEMFCs) have been widely investigated as power sources for the future, particularly for vehicular and stationary applications. In the past, PEMFCs have been restricted to low-temperature (< 80 °C) operation, due to the limitations associated with the Nafion® membrane typically used in such fuel cells. The Nafion® membrane requires a high degree of saturation to effectively conduct protons, hence its performance decreases drastically above 100 °C. As a result, the inlet gas streams must be well humidified in order to maintain proper water balance in low temperature fuel cells.

Recently, there has been growing interest in operating PEMFCs at elevated temperatures (120–200 °C) and low humidity (25–50% RH). This way, there is no need for external humidification and cooling. In addition, high temperature operation precludes the nagging problems associated with liquid water management. Alternative membranes are needed, which maintain mechanical, chemical and thermal properties at elevated temperatures, and which are able to conduct protons in low humidity environments.

One such membrane, which has been investigated, is polybenzimidazole (PBI) [1]. PBI is typically doped with phosphoric acid to attain proton conductivity. Phosphoric acid systems have the advantage of good stability at elevated temperatures, and being highly ionizing, is very conductive to protons [2]. One disadvantage, however, is its relatively poor transport of dissolved gases [3–5]. Another drawback is that phosphoric acid anions tends to adsorb onto the platinum (Pt) catalyst, thereby reducing its effective surface area for electrochemical reactions [4]. To date, no suitable alternative doping agent has been identified, which: (1) is highly ionizing, (2) is stable at high temperatures, (3) has a low propensity to adsorb onto the catalyst, and (4) offers good transport characteristics for dissolved gases.

Mathematical modeling is a crucial element in the development of fuel cell technology. Modeling is intended to gain fundamental insights into the processes occurring within the fuel cell, which cannot be experimentally ascertained with the current state of the art. In addition, modeling may highlight areas where research should be focused, hence speeding up the development process. Numerous models have been developed for low temperature PEMFCs [6]. However, with the paradigm shift toward higher temperature operation, there is need for modeling of such fuel cells. The only models of intermediate temperature fuel cells developed, to date, are the ones by the present

* Corresponding author. Tel.: +1 786 877 9235; fax: +1 305 348 1932.
E-mail addresses: dcheddie@yahoo.com (D.F. Cheddie), norman.munroe@arc.fiu.edu (N.D.H. Munroe).

0360-3199/$ - see front matter © 2006 International Association for Hydrogen Energy. Published by Elsevier Ltd. All rights reserved.
doi:10.1016/j.ijhydene.2006.10.061

Nomenclature

a	effective surface area, m^{-1}
c_p	specific heat capacity at constant pressure, $J\,kg^{-1}\,K^{-1}$
C	concentration, $mol\,m^{-3}$
d	diameter, m
D	species diffusivity, $m^2\,s^{-1}$
D_T	effective thermal diffusivity, $m^2\,s^{-1}$
F	Faraday constant, $96487\,C\,mol^{-1}$
H	Henry's constant, $mol\,m^{-3}\,atm^{-1}$
i	current density, $A\,m^{-2}$
i_0	exchange current density, $A\,m^{-2}$
j	reaction rate, $A\,m^{-3}$
k	thermal conductivity, $W\,m^{-1}\,K^{-1}$
k_p	gas permeability, m^2
m	mass fraction, mass loading, $kg\,m^{-2}$
M	molar mass, $kg\,mol^{-1}$; molarity, $mol\,l^{-1}$
P	pressure, Pa
R	universal gas constant, $8.3143\,J\,mol^{-1}\,K^{-1}$
S	source, entropy
T	temperature K
u	velocity, $m\,s^{-1}$
V	potential, V
x	mole fraction
X	doping level
α	charge transfer coefficient
γ	concentration parameter
ε	porosity, volume fraction
η	electrode polarization
θ	blockage factor
μ	dynamic viscosity, Pa s
ρ	density, $kg\,m^{-3}$
σ	electrical or ionic conductivity, $S\,m^{-1}$
ϕ	electrical or ionic potential, V

Subscripts

a	anode
c	cathode
e	electrolyte phase
f	fluid property
i, j	species i, j
m	mass quantity
s	solid phase
T	thermal

Superscripts

d	dispersion
eff	effective

authors [7–12]. Our previous models range from 1D to 3D, but are all single phase models that consider only gas interactions.

The present model improves on the previous ones by considering a two phase media. There is still no liquid phase, due to the temperatures of operation. Nevertheless, it has been shown that reacting gases (oxygen and hydrogen) must first dissolve in the electrolyte before undergoing electrochemical reaction [13]. The present model accounts for gaseous dissolution into the aqueous phase. Unlike the previous models, which assumed gas phase kinetics, this model assumes aqueous phase kinetics. It is a comprehensive model, which accounts for all transport and polarization effects. Model predictions are validated by experiments performed by Qingfeng et al. [14]. After model validation, parametric analyses are presented which investigate the effects of acid doping level, temperature, catalyst activity, catalyst layer thickness, and transport properties of dissolved gases on fuel cell performance.

2. Model development

2.1. Physical description

Fig. 1 (not drawn to scale) shows a two-dimensional schematic of a fuel cell with seven major subdomains: the anode and cathode gas channels, gas diffusion layers, catalyst layers, and the PEM/electrolyte. In this paper, the membrane considered is PBI doped with phosphoric acid.

Hydrogen and oxygen are supplied, respectively, to the anode and cathode gas channels. Some of the flow in the channels permeates the porous gas diffusion layers, where it is transported, primarily by diffusion, to the catalyst layers. The gases then dissolve in the electrolyte phase, which "wets" the catalyst, after which they diffuse to the Pt sites where the following half cell reactions take place:

$$H_2(aq) \rightarrow 2H^+(aq) + 2e^- \quad \text{(anode)}, \tag{1}$$

$$\tfrac{1}{2}O_2(aq) + 2H^+(aq) + 2e^- \longrightarrow H_2O\ (aq)\ \text{(cathode)}. \tag{2}$$

The protons (H^+) ions, produced at the anode, flow across the membrane, via a Grothus mechanism [15], to the cathode where it reacts with oxygen. The electrons flow around in an external circuit. The current is generated by the movement of the electrons, which flow under the influence of the potential difference created between the two electrodes. There is also an electrolyte phase current resulting from the flow of protons, which will be discussed later.

Fig. 2 shows a schematic of the catalyst layer. The catalyst layer is a fused region between the membrane and the diffusion layer, with sputtered Pt particles. An effective catalyst layer contains electrolyte phase for the transport of protons and dissolved gases, solid (carbon) regions for the flow of electrons, and sputtered Pt particles, on the surface of which electrochemical reactions occur. For the purpose of analysis, the catalyst layer is assumed to be a homogeneous region where electrolyte

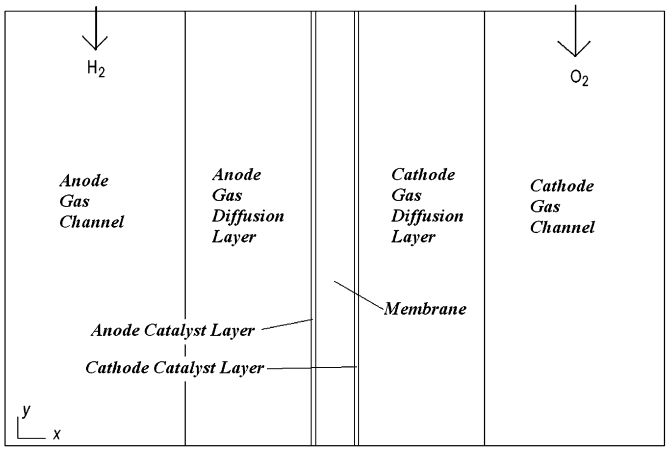

Fig. 1. 2D computational domain.

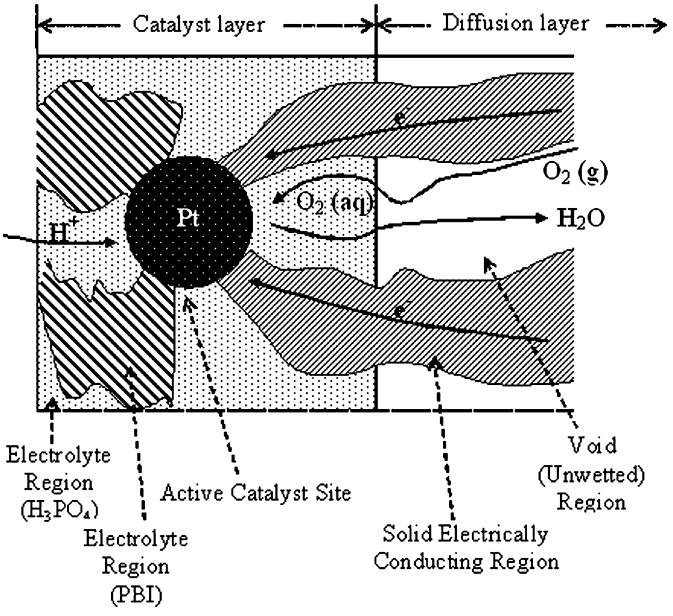

Fig. 2. Schematic of the cathode catalyst layer.

and solid regions are well connected to the evenly distributed catalyst particles.

2.2. Governing equations

This section details the governing equations which are used to model the phenomena described above. The bulk flow in the gas channels, is laminar due to the low velocities typical in fuel cells, and hence is governed by the Navier Stokes equations. The flow in the porous diffusion layers is characterized as Darcy flow, and hence Darcy's law may be used to model it. The flows in both the channels and the diffusion layers may be combined by incorporating the Darcy's law source term in the Navier Stokes equations, which apply only in the porous regions:

$$\rho u \cdot \nabla u = -\nabla P + \nabla \cdot (\mu \nabla u) - \frac{\mu}{k_p} u, \tag{3}$$

$$\nabla \cdot (\rho u) = 0. \tag{4}$$

There is no consumption or generation of species in the gas flow regions, hence continuity of the fluid flow exists (Eq. (4)). The transport of individual gas species is governed by the Stefan Maxwell equations:

$$\rho u \cdot \nabla m_i = \nabla \cdot \left[\rho \varepsilon m_i \sum_{j=1}^{N} D_{i,j}^{\text{eff}} \left\{ \frac{M}{M_j} \left(\nabla m_i + m_i \frac{\nabla M}{M} \right) \right\} \right]. \tag{5}$$

At the catalyst layers, the gas species dissolve in the acid doped electrolyte. It is assumed that there is no net translation of the electrolyte medium, hence the transport of dissolved species is purely diffusive, and governed by Fick's law:

$$\nabla \cdot (-D_i^{\text{eff}} \nabla C_i) = S_i. \tag{6}$$

Due to the flow of charged species, and the exothermic nature of the fuel cell reactions, heat is generated within the cell. The energy equation accounts for convection, conduction and heat generation due to ohmic or Joule heating, as well as heat of reaction:

$$\rho c_p u \cdot \nabla T = \rho c_p \nabla \cdot (D_T \nabla T) + S_T, \tag{7}$$

$$S_T = S_{\text{ohm}} + S_{\text{rxn}}. \tag{8}$$

Due to the flow of electrons and protons within the cell, there are associated solid phase and electrolyte phase currents and potentials, respectively. The charge conservation equations in the both phases are given by

$$\nabla \cdot i_s = \nabla \cdot (-\sigma_s^{\text{eff}} \nabla \phi_s) = -j, \tag{9}$$

$$\nabla \cdot i_e = \nabla \cdot (-\sigma_e^{\text{eff}} \nabla \phi_e) = +j, \tag{10}$$

$$j = a i_0^{\text{ref}} \left(\frac{C_i}{C_{\text{ref}}} \right)^{\gamma_i} \left\{ \exp\left[\frac{\alpha_F}{RT} \eta \right] - \exp\left[\frac{(1-\alpha)_F}{RT} \eta \right] \right\}. \tag{11}$$

The quantity, j, may be considered the local reaction rate, and is defined as the rate of charge transfer between the solid and electrolyte phases. C_{ref} is the reference reactant concentration at which the exchange current density, i_0, is reckoned. This is usually the saturation concentration at 1 atm. The effective surface area, a, is defined as the ratio of the total active catalyst surface area to the total catalyst region volume, and thus takes into account surface roughness in the catalyst layer. The Butler–Volmer equation (11) states that the rate of electrochemical reaction is driven by the difference in potential between the two respective phases, and is affected by the concentration of reactants at the catalyst sites.

2.3. Source terms

The source terms depend on the reaction rate in each catalyst layer and the stoichiometry of the overall cell reaction. With the exception of the ohmic heating term, all other source terms are non-zero only in the catalyst layers. The reaction rate, j, is positive in the anode catalyst layer and negative in the cathode. Thus, the following equations define the local rates of oxygen

consumption, water vapor production, hydrogen consumption, reactive heat and ohmic heat generation:

$$S_{O_2} = \frac{j}{4F}\ (\mathrm{mol\,m^{-3}\,s^{-1}}), \tag{12}$$

$$S_{H_2O} = -\frac{j}{2F}\ (\mathrm{mol\,m^{-3}\,s^{-1}}), \tag{13}$$

$$S_{H_2} = -\frac{j}{2F}\ (\mathrm{mol\,m^{-3}\,s^{-1}}), \tag{14}$$

$$S_{rxn} = -j\left(\phi_e - \phi_s - \frac{T\Delta S}{n^F}\right)\ (\mathrm{W\,m^{-3}}), \tag{15}$$

$$S_{ohm} = \frac{i_s^2}{\sigma_s^{eff}} + \frac{i_e^2}{\sigma_e^{eff}}\ (\mathrm{W\,m^{-3}}). \tag{16}$$

2.4. Boundary conditions

In the y-direction, the computational domain spans the length of the gas channels passing over the membrane electrode assembly (MEA). At the inlet of the gas channels, the flow velocity, temperature and species mass fractions are specified according to the supply conditions. In the experimental work of Qingfeng et al. [14], pure un-humidified hydrogen and oxygen are supplied to the cell at flow rates of 160 ml $\mathrm{min^{-1}}$under one atmosphere of pressure. This translates to an inlet y-velocity of $0.16\,\mathrm{m\,s^{-1}}$ and hydrogen and oxygen mass fractions of unity. The pressure at the outlet of the flow channels is specified at one atmosphere and convective flux boundary conditions are specified for the species and thermal equations. Every other boundary in the y-direction is considered to be thermally insulated or impervious to fluid flow, hence Neumann boundary conditions apply.

In the x-direction, the domain spans the anode gas channel to the cathode gas channel. No slip boundary conditions are specified at the gas channel outer walls, which are also impervious to species flow and thermally insulated (assumed). At the diffusion layer/catalyst layer interfaces, there are phase changes between gaseous and aqueous/dissolved species. There is continuity of flux between the gaseous and aqueous species, i.e. $\rho(-D_i^{gas}\nabla m_i + u m_i) = -M_i D_i^{aq}\nabla C_i$. In addition, the concentration of dissolved species at the interface is related, by Henry's Law, to the partial pressure of the gas at the same interface, i.e. $C_i = \mathrm{H}_i P_i$.

The solid phase electrical potential is set to zero at the anode gas channel/diffusion layer interface, and to the cell voltage at the cathode gas channel/diffusion layer interface. Since no electrons flow through the membrane, the solid phase potential gradient is set to zero at the membrane/catalyst layer interfaces. The electrolyte phase potential gradient is set to zero at the catalyst layer/diffusion layer interfaces since protons cannot flow through the diffusion layer.

2.5. Constitutive relations

The most significant factor affecting the performance of a PBI membrane is the acid doping level. When PBI is doped or immersed in phosphoric acid, the latter is absorbed into the polymer matrix, forming a single phase material [1]. The doping level, X, is defined as the number of moles of acid absorbed per PBI repeat unit. The PBI repeat unit contains two bonding sites for phosphoric acid, thus two moles of acid per repeat unit can be bonded to PBI. However, it is possible for the doping level to exceed 2. Any additional absorbed acid is termed free or unbonded acid. It forms an amorphous phase within the polymer matrix. It is believed that the transport of protons and dissolved gases takes place in the free acid inside the PBI matrix [13].

The doping level is a function of the concentration of acid used in the doping process, an equilibrium being established between the acid absorbed into the polymer matrix and the acid in the immersion solution. The following correlation exists between the doping level and the phosphoric acid concentration, where M is the concentration ($\mathrm{mol\,l^{-1}}$) of the acid solution [16]:

$$X = 0.012M^3 - 0.2111M^2 + 1.2363M + 0.7119. \tag{17}$$

The volume fraction of amorphous phosphoric acid in the membrane is related to the number of moles of free acid present [13] in accordance to the following equation:

$$\varepsilon_{PA} = \left(\frac{4.81}{X-2} + 1\right)^{-1}. \tag{18}$$

The amount of phosphoric acid within the membrane is determined by the concentration of the acid solution used during the doping procedure. As a result, water is also absorbed by the membrane producing a phosphoric acid solution within the membrane (as opposed to pure phosphoric acid). In addition, the concentration of the acid within the membrane depends on the operating conditions. As a consequence, an equilibrium is established between the humidity in the environment and the water inside the membrane. It is shown that for most fuel cell applications, the acid concentration within the membrane ranges from 85 to 95 w% phosphoric acid [13,16].

The membrane ionic conductivity is related to both the temperature and the doping level. The conductivity may also depend on the humidity, in as much as the humidity affects the acid concentration in the membrane. The following relation is used, in this work, to determine the membrane conductivity [14],

$$\sigma_m = \frac{100}{T}\exp\left[8.0219 - \left(\frac{2605.6 - 70.1X}{T}\right)\right]\ \mathrm{S\,m^{-1}}. \tag{19}$$

The transport and electro-kinetic properties of the electrolyte are also related to the doping level. Liu et al. [13] show that the effective diffusivity of oxygen in the acid doped electrolyte is related to the diffusivity of the amorphous phosphoric acid by a Bruggeman relation,

$$D_{O_2}^{(PBI)} = D_{O_2}^{(PA)}\varepsilon_{PA}^{1.8}. \tag{20}$$

The Henry's constant pertaining to oxygen solubility in acid doped PBI is also related to the solubility in amorphous

phosphoric acid [13]:

$$H_{O_2}^{(PBI)} = \varepsilon_{PA}^{1.945}\left[H_{O_2}^{(PA)} + 5.79(1-\varepsilon_{PA}^{1.8})\right] \text{ mol m}^{-3}\text{ atm}^{-1}. \quad (21)$$

The transport properties of oxygen in concentrated phosphoric acid are related to the temperature and the acid concentration (mass fraction) [17]:

$$\ln(10^9 D_{O_2}) = (-192.55\, m_{PA}^2 + 323.55\, m_{PA} - 125.61) + \frac{62010\, m_{PA}^2 - 105503\, m_{PA} + 40929}{T} \text{ m}^2\text{ s}^{-1}, \quad (22)$$

$$\ln(10 H_{O_2}) = (257.13\, m_{PA}^2 - 431.08\, m_{PA} + 178.45) + \frac{-93500\, m_{PA}^2 + 156646\, m_{PA} - 64288}{T} \text{ mol m}^{-3}\text{ atm}^{-1}. \quad (23)$$

The exchange current density for the oxygen reduction reaction over a Pt catalyst in contact with acid doped PBI, is related to that in a phosphoric acid solution [13]:

$$\log(i_0^{(PBI)}) = \log(i_0^{(PA)}) - 4.16(1-\varepsilon_{PA})\, A\text{ m}^{-2}. \quad (24)$$

The exchange current density in 85 wt% phosphoric acid is described by Huang et al. [5]:

$$\log(i_0^{(PA)}) = 3.509 - \frac{2193}{T} \text{ A m}^{-2}. \quad (25)$$

Although much attention has been given to properties affecting the oxygen reduction reaction at the cathode, not much has been devoted to the oxidation of hydrogen at the anode. It has been traditionally assumed that the hydrogen reaction is fast, and hence does not warrant much research. As a result, data for the transport properties of hydrogen in phosphoric acid systems are not readily available. It is assumed, in this work, that the solubility of hydrogen in phosphoric acid is four times that of oxygen, and its diffusivity is twice as much, as is the case with water systems [18]. It will be assumed that the exchange current density for the anode reaction is 10^9 times that at the cathode.

It can be shown geometrically that the effective surface area per unit volume of the catalyst region (or per agglomerate volume) is given by the following expression, where θ is a blockage factor:

$$a = \frac{6\, m_{Pt}}{\rho_{Pt} d_{Pt} L_{cat}}(1-\theta). \quad (26)$$

There are numerous causes of catalyst blockage. CO adsorbed onto the catalyst may block hydrogen. Liquid water may block the oxygen. But at elevated temperatures, CO poisoning becomes less significant and liquid water does not exist. The only cause of blockage considered in this model is the adsorption of phosphoric acid anions onto the catalyst sites. This reduces the effective surface area of the catalyst, thus reducing its activity. This blockage is not as yet quantitatively understood, nevertheless it is believed to be a function of acid concentration, temperature, and electrode overpotential. The following relation is obtained from data presented by Zelanay et al. [4] to quantify the blockage factor in this model:

$$\theta = -0.893\,\eta^2 + 1.714\,\eta. \quad (27)$$

This is based on experiments performed at 25 °C in a 0.02 M phosphoric acid solution. The blockage decreases with temperature, but increases with acid concentration, so in the absence of other experimental data, this correlation will be used in this model.

Other constitutive relations, such as the correction of fluid and material properties for porous media, are the same as in Cheddie and Munroe [10].

2.6. Computer hardware

The governing equations, with applicable boundary conditions, are solved using the coupled multi-physics software, FEMLAB 3.1i. The domain is divided into approximately 80,000 s order triangular finite elements. The mesh is especially dense on the outer surface of the catalyst layers, which is necessary to accurately model the sharp concentration gradients existing there. Computations were conducted on a 64 bit Linux platform with a 4 GB, 3.8 GHz processor. Computations required up to 2 h of processing time to generate data for each current–voltage (IV) curve.

3. Results and discussion

3.1. Model validation

Tables 1–3 list the numerical values used in this work, in addition to the equations in the previous section. Fig. 3 compares the model predictions with corresponding experimental data [14] at 150 and 170 °C. It shows a good fit for the 150 and 170 °C data. The concentration overpotential regions occur mainly due to the blockage caused by the adsorption of

Table 1
Base case membrane and diffusion layer properties (423 K)

Membrane		
Thermal conductivity, k_m [19]	40	W m^{-1} K^{-1}
Doping level, X	6.2	
Ionic conductivity, σ_m	4.25	S m^{-1}
Thickness	8×10^{-5}	m
Cross section	5×10^{-4}	m^2
Diffusion layer (*Graphite*) [18]		
Thermal conductivity, k_d [20]	1.15	W m^{-1} K^{-1}
Electrical conductivity, σ_d	120	S m^{-1}
Porosity, ε	0.4	
Permeability, k_p	1.8×10^{-11}	m^2
Thickness	2.5×10^{-4}	m
Channels [14]		
Channel length	0.0225	m
Channel width	7.5×10^{-4}	m

phosphoric acid anions (Eq. (27)). Fig. 3 shows that at the higher temperatures, this blockage is more pronounced, possibly because its effect is more significant as the current density increases. According to Eq. (27), the actual fraction of the blocked catalyst surface area is the same at any given cell polarization, however, the effect of the blockage may be more significant as the current density increases. Physically, at higher current densities, there is a higher reaction rate, hence a greater demand for catalyst surface area. Thus at higher current densities, the effect of the blockage is more strongly "felt".

Table 2
Catalyst layer properties at 423 K

	Anode	Cathode	
ai_0^{ref}	1.27×10^{13}	1.27×10^{4}	A m^{-3}
Diffusivity, D_i	3.36×10^{-10}	1.68×10^{-10}	m^2 s^{-1}
Solubility, H_i	3.20	0.80	mol m^{-3} atm^{-1}
α [18]	0.5	2	
γ [18]	0.5	1	
Thickness, L_{cat}	1×10^{-5}		m
Loading, m_{Pt}	4.5×10^{-3}		kg m^{-2}
Particle diameter, d_{Pt}	1×10^{-9}		m

Table 3
Fluid properties at 423 K [21,22]

	Oxygen	Water vapor	Hydrogen	
M	32×10^{-3}	18×10^{-3}	2×10^{-3}	kg mol^{-1}
k	0.036	0.030	0.239	W m^{-1} K^{-1}
c_p	956	1980	14500	J kg^{-1} K^{-1}
μ	27×10^{-6}	14×10^{-6}	1.1×10^{-6}	Pa s
α	44.4×10^{-6}	30.8×10^{-6}	217×10^{-6}	m^2 s^{-1}
$D_{i,j}$	41.9×10^{-6}			m^2 s^{-1}

3.2. Parametric analyses

The membrane doping level of 6.2 with the fuel cell operating at 150 °C, and all the other conditions listed in Tables 1–3 will be considered the base case. In this section, we vary the main parameters affecting the fuel cell to observe the effect on the performance, as predicted by the model.

Fig. 3 also shows the model predictions at 110 and 130 °C although experimental results were not given for those temperatures. The exchange current density, reactant solubility and diffusivity, and membrane conductivity all increase with temperature, hence the performance of the fuel cell improves with temperature. In every case, the cell power density peaks at approximately 0.4 V. At 110 °C, the peak power density predicted is 1.35 kW m^{-2}, while the peak value at 170 °C is 3.67 kW m^{-2}, nearly three times as much. The model predicts that the peak power output increases by 25–50% for a temperature increase of 20 °C within the temperatures range, 110–170 °C.

Fig. 4 shows the predicted performance as the membrane doping level is varied. As expected the fuel cell performance increases with doping level, because at higher doping levels, there is a greater amount of amorphous phosphoric acid present in the membrane, leading to higher membrane conductivities. The exchange current density and the transport properties also increase slightly with doping level, thus augmenting the performance enhancement. The peak power output increases by 38% as the doping level is increased from 6.2 to 8. In fact, the performance of the cell with a doping level of 8 at 150 °C (Fig. 4), is better than that of the cell with doping level 6.2 at 170 °C (Fig. 3). So increasing the doping level can have the same effect as increasing the temperature. This is especially useful information for vehicular applications, where an upper limit for the desired temperature exists. It should be noted, though, that at excessively high doping levels (> 10), the mechanical properties of the membrane begin to degrade.

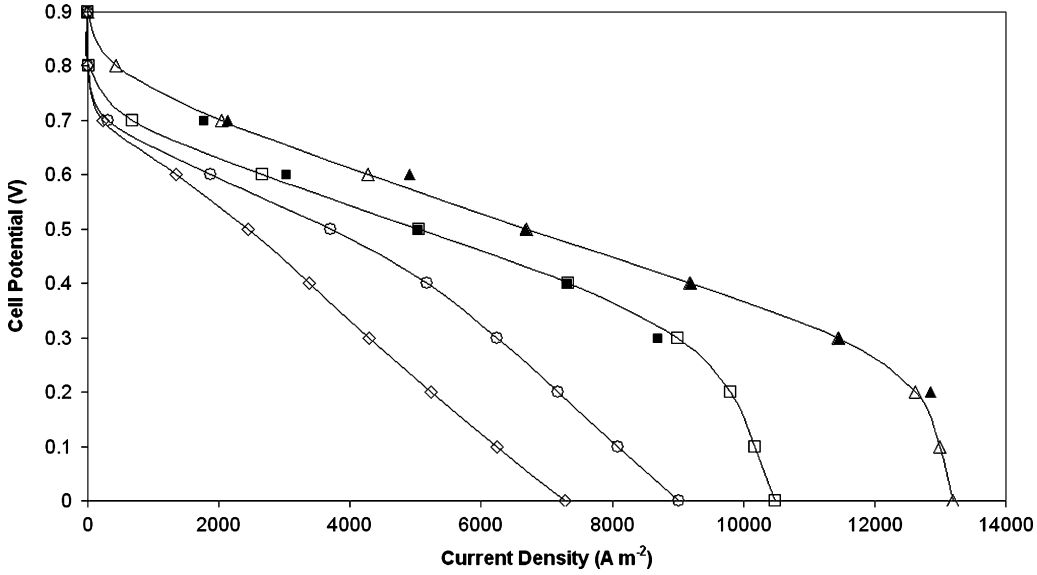

Fig. 3. Polarization curves as a function of temperature. ◇—model (110 °C), ○—model (130 °C), □—model (150 °C), △—model (170 °C), ■—experimental (150 °C), and ▲—experimental (170 °C).

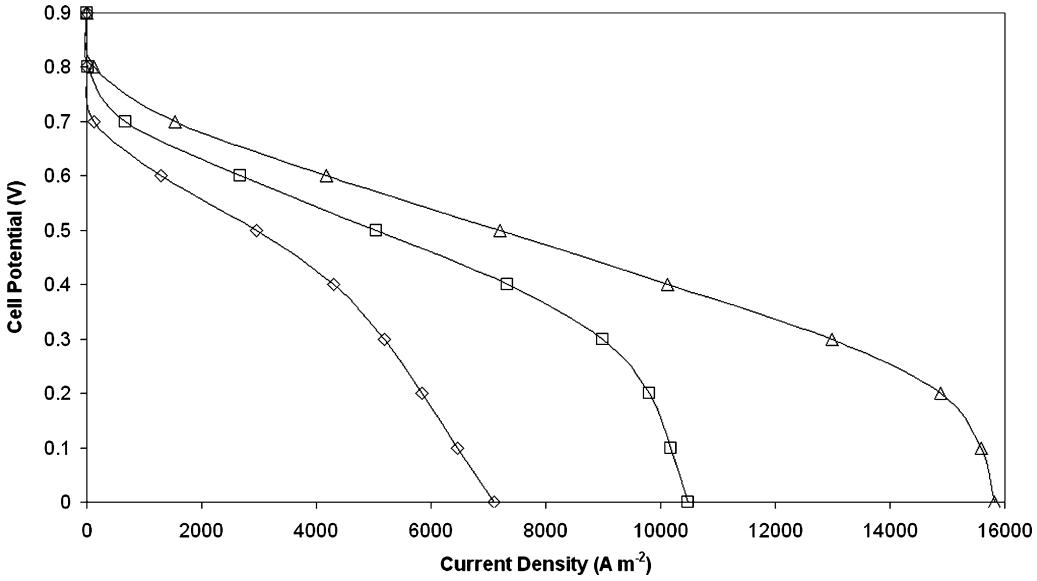

Fig. 4. Polarization curves as a function of acid doping level: ◇ ($X = 4.5$), □ ($X = 6.2$), and △ ($X = 8$).

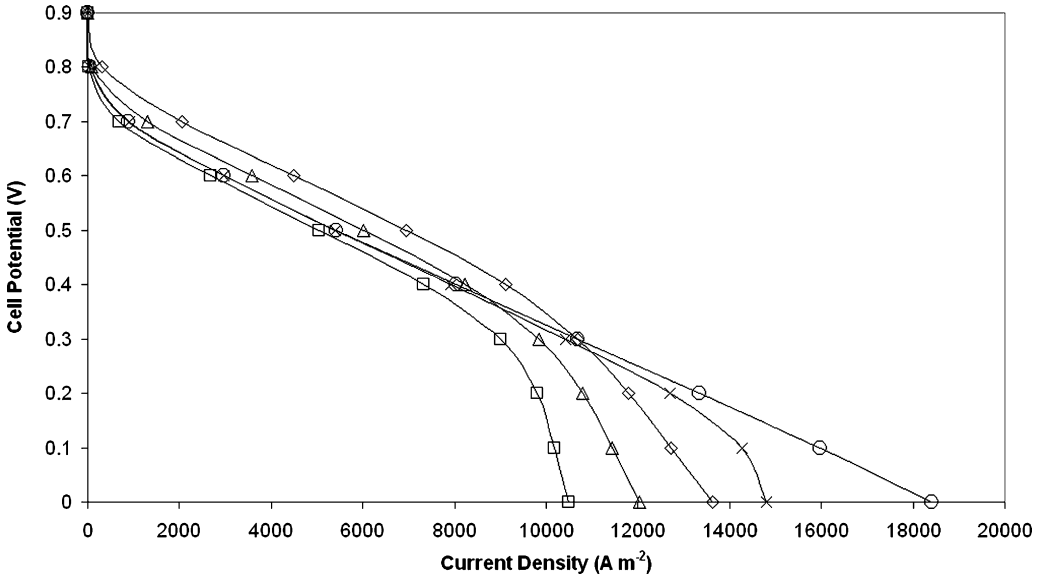

Fig. 5. Polarization curves as a function of exchange current density: □ (base); △ (10 times $i_{0,c}$); ◇ (100 times $i_{0,c}$); × (10 times $i_{0,a}$); and ◯ (100 times $i_{0,a}$).

Fig. 5 shows the effects of varying the cathode and anode exchange current densities, $i_{0,c}$ and $i_{0,a}$ from their base values. Increasing the exchange current density can be achieved by reducing the diameter, hence increasing the surface area of the catalyst particles, or by distributing the catalyst over a thinner layer (see Eq. (26)). It is usually expected that the fuel cell performance is much more sensitive to $i_{0,c}$ than $i_{0,a}$, because the hydrogen oxidation reaction is much faster than the oxygen reduction reaction.

Generally it is seen that increasing $i_{0,c}$ by a factor of 10 results in approximately a 10% increase in peak power output. Increasing $i_{0,a}$ by a factor of 10 from its base value results in an 8% initial increase in peak power. Further increasing it by a factor of 10 results in a 1% increase in power. This is because as $i_{0,a}$ is increased, the anode polarization decreases. The effect of increasing $i_{0,a}$ becomes smaller as it is increased beyond a certain limit. Another notable feature of this figure, is that increasing $i_{0,a}$ results in a more significant increase in limiting current density, than is the case when $i_{0,c}$ is increased. This is explained later.

Fig. 6 sheds more light on these trends. It shows the variation of the solid phase and electrolyte phase potentials across the catalyst layers and the membrane for the base case condition at a cell voltage of 0.4 V (peak power operation). The activation overpotential at the catalyst layers is defined as the deviation between the reversible electrode potential (~1.154 V at the

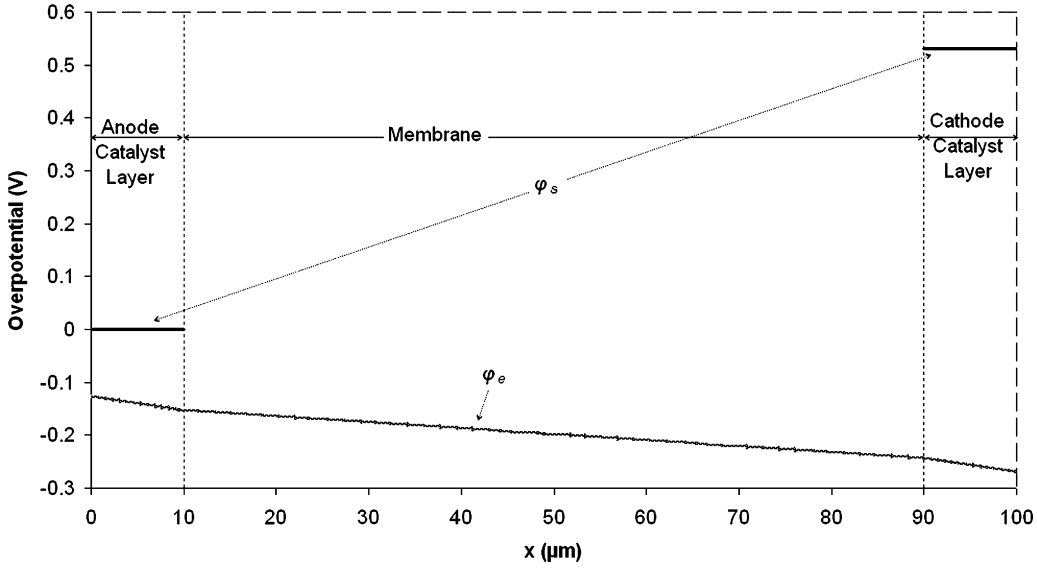

Fig. 6. Solid and electrolyte potential variations across the cell.

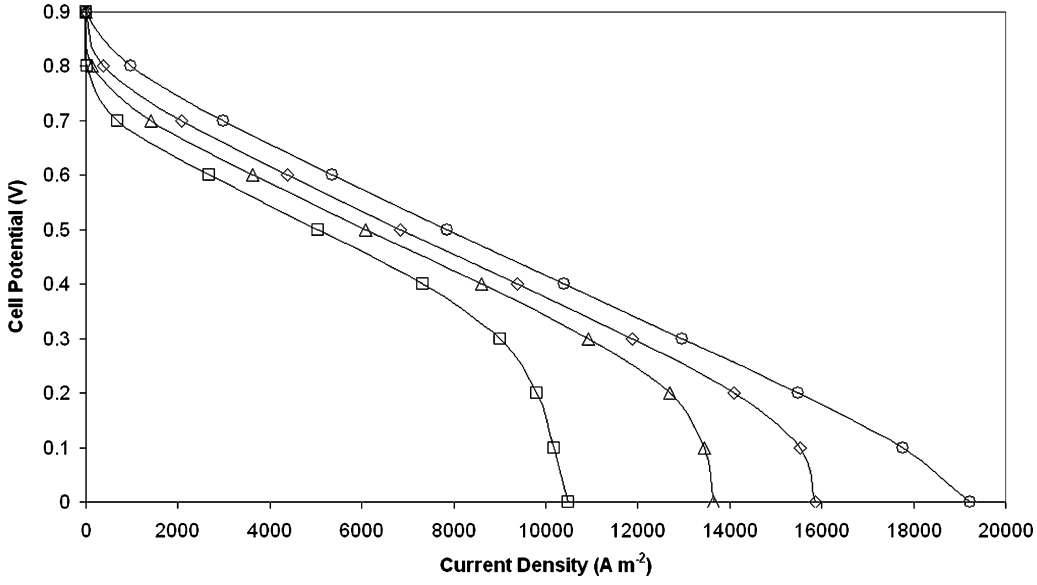

Fig. 7. Polarization curves as a function of transport properties: □ (base), △ (2.5 times H_i), ◇ (25 times D_i), and ◯ (2.5 times H_i and 25 times D_i).

cathode) and the magnitude of the difference between the two phase potentials. The anode activation overpotential is 0.12 V while the cathode activation overpotential is 0.35 V. Normally the overpotential at the anode is less than 0.05 V, which is why increasing the anode activity does not usually improve the performance significantly. In this case, there is a relatively large anode polarization, hence increasing the exchange current density results in a large improvement in performance. As the anode polarization decreases, further increasing the exchange current density results in a smaller improvement in performance, as predicted by the model. These results indicate that the anode polarization is not negligible, at least for phosphoric acid systems, and there is much room for performance enhancement by improving the anode performance.

Fig. 7 shows the IV performance as the transport properties of the catalyst layers are improved. It is reported that oxygen has 2.5 times higher solubility and 25 times higher diffusivity in CF_3SO_3H than in H_3PO_4 [4]. So these values were inputted to the model, with all other quantities remaining unchanged from the base condition, to observe the effect on the performance. As the solubility of dissolved gases in the electrolyte increases by 2.5 times, the peak power output increases by 17%. Increasing the diffusivity 25 times results in a 28% increase in peak performance. A combination of both results in a 42% improvement in performance.

A higher solubility implies that the concentration of the dissolved gases in the electrolyte is higher, and hence the reaction rate is faster (Eq. (11)). A higher diffusivity implies that the

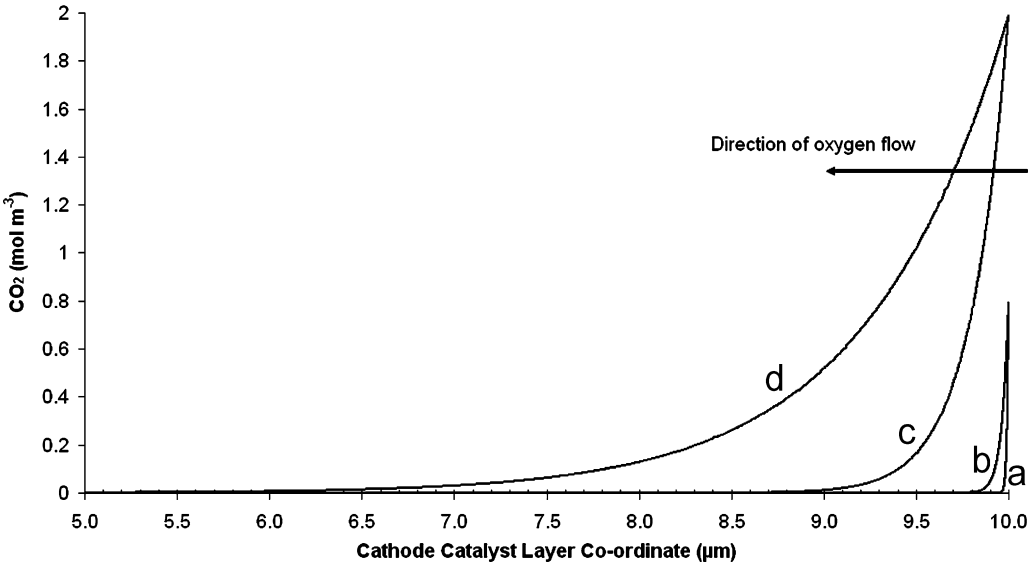

Fig. 8. Oxygen concentration in the outer 5 μm of the cathode catalyst layer: (a) base case, 0.4 V, (b) base case 0.7 V, (c) 2.5 times H_i and 25 times D_i, 0.4 V, and (d) 2.5 times H_i and 25 times D_i, 0.7 V.

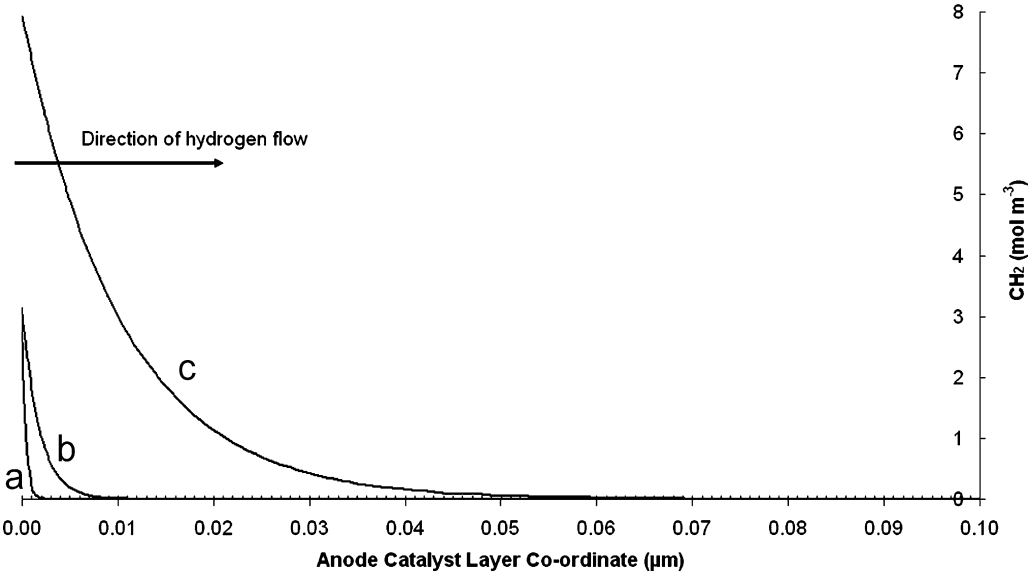

Fig. 9. Hydrogen concentration in the outer 0.1 μm of the anode catalyst layer: (a) base case, 0.4 V, (b) base case 0.7 V, (c) 2.5 times H_i and 25 times D_i, 0.4,V.

dissolved gases are better able to permeate the catalyst layer. Figs. 8 and 9 shed more light on why the performance increases as the transport properties are enhanced. Fig. 8 shows the oxygen concentration variation in the outer half (5 μm) of the cathode catalyst layer. As oxygen enters from the right, the initial concentration is related to the partial pressure of the gas at the interface. For the base case at 0.4 V (a), the concentration quickly falls to zero (as oxygen is consumed in the electrochemical reactions) within the outer 0.1 μm of the catalyst layer. This means that 99% of the catalyst is unutilized. Once the concentration falls to zero, no more reaction takes place (Eq. (11)). This sharp decrease in concentration is due to two effects: the low diffusivity ($\sim 10^{-10}\,m^2\,s^{-1}$) and the high reaction rate. As the cell voltage is increased to 0.7 V (b), the reaction rate is smaller since less current is produced, and consequently the oxygen is able to permeate a little further into the catalyst layer. When the solubility and diffusivity increase (c and d), the oxygen is able to permeate even further into the catalyst layer, hence better catalyst utilization is achieved. For the high solubility and diffusivity case operating at 0.4 V (optimum conditions), the outer 10–15% of the catalyst is utilized.

Fig. 9 shows the equivalent plots for the dissolved hydrogen concentration on the outer 0.1 μm (1%) of the anode catalyst layer. The catalyst utilization at the anode is even worse, primarily due to the higher reaction rates. For the base case, the reactions take place on the outer 0.05% of the catalyst layer,

with 99.95% of the catalyst being wasted. As the solubility and diffusivity increase, the hydrogen is able to permeate further into the catalyst layer, but still the catalyst utilization is less than 1%. This helps to explain why an improvement in performance is expected when the transport properties increase.

Because of the low solubility and diffusivity of phosphoric acid systems, significant transport limitations exist at both electrodes. It was seen in Figs. 8 and 9, that the transport limitations are more severe at the anode than the cathode. This may explain why the limiting current increases significantly when the anode exchange current density increases (Fig. 5). So the model predicts that the fuel cell performance can be considerably improved if an alternative doping agent to phosphoric acid can be found, which has higher transport properties, comparable ionic conductivity, and similar stability at high temperatures.

The model results also raise another issue that warrants further research. Figs. 8 and 9 showed that a miniscule fraction of the catalyst is actually utilized in electrochemical reactions, since the reactants cannot permeate very far into the catalyst layer. Typically $0.5\,mg\,cm^{-2}$ of catalyst are loaded onto the electrodes, and usually after assembly, the catalyst region develops a thickness in the order of 10 μm. It is intuitive that if, instead, $0.05\,mg\,cm^{-2}$ of Pt were loaded over a 1 μm thickness, then the fuel cell performance would be unaffected, since the inner 90–99% of the catalyst layer is unutilized anyway. But although the performance would not change, 90% of the cost of the catalyst would be saved. If it were further possible to load $0.005\,mg\,cm^{-2}$ of Pt over a 0.1 μm thickness at the anode, then once again the fuel cell performance would be unchanged, but a 99% catalyst cost reduction would be realized. Considering that the Pt catalyst is one of the most expensive elements in the PEMFC, this is a very useful revelation. With the emergence of nano-fabrication technologies, the ability to distribute the catalyst over such narrow regions may not be unrealistic, and may be a crucial step in the commercialization of fuel cell technology.

4. Conclusions

A two-phase two-dimensional model of an intermediate temperature PEM fuel cell was presented. The model attempted to simulate experimental results produced using a fuel cell equipped with a phosphoric acid doped PBI membrane. The model was able to predict the polarization performance, as well as the transport characteristics within the cell. The polarization results matched well with the experimental results at 150 and 170 °C.

Parametric analyses were then performed, from which the following conclusions were drawn: (1) increasing the acid doping level of the membrane has more or less the same effect as increasing the temperature of operation, so high performance could be achieved without using excessively high temperatures (→ 200 °C). (2) Significant anode polarization occurs in this type of fuel cell, evidenced by the fact that significant improvements in limiting current occurred as the anode exchange current density increased. (3) Significant transport limitations exist at both electrodes, due to the low diffusivity and solubility of phosphoric acid systems. (4) Catalyst utilization is less than 1%, implying that significant cost reductions are possible through more advanced catalyst deposition techniques.

Acknowledgment

The authors are grateful for the FIU Graduate School Dissertation Fellowship, and to Gas Technology Institute (Contract Number 8390) for their support of this work.

References

[1] Wainright JS, Wang JT, Weng D, Savinell RF, Litt M. Acid-doped polybenzimidazoles: a new polymer electrolyte. J Electrochem Soc 1995;142:L121.
[2] Bouchet R, Miller S, Duclot M, Souquet JL. A thermodynamic approach to proton conductivity in acid-doped polybenzimidazole. Solid State Ionics 2001;145:69–78.
[3] Scharifker BR, Zelenay P, Bockris J. The kinetics of oxygen reduction in molten phosphoric acid at high temperatures. J Electrochem Soc 1987;134:2714.
[4] Zelenay P, Scharifker BR, Bockris JOM, Gervasio G. A comparison of the properties of CF_3SO_3H and H_3PO_4 in relation to fuel cells. J Electrochem Soc 1986;133:2262.
[5] Huang JC, Sen RK, Yeager E. Oxygen reduction on platinum in 85% orthophosphoric acid. J Electrochem Soc 1979;126:786.
[6] Cheddie D, Munroe N. Review and comparison of approaches to proton exchange membrane fuel cell modeling. J Power Sources 2005;147:172.
[7] Cheddie D, Munroe N. Parametric model of an intermediate temperature PEMFC. J Power Sources 2006;156:414.
[8] Cheddie D, Munroe N. Mathematical model of a PEMFC using a PBI membrane. Energy Convers Manage 2006;47:1490–504.
[9] Cheddie D, Munroe N. Two-dimensional effects in intermediate temperature PEMFCs. Int J Trans Phenom 2006;8:51.
[10] Cheddie D, Munroe N. Three-dimensional modeling of high temperature PEMFCs. J Power Sources 2006;160:215.
[11] Cheddie D, Munroe N. Analytical correlations for intermediate temperature PEMFCs. J Power Sources 2006;160:299.
[12] Cheddie D, Munroe N. Computational modeling of PEM fuel cells with PBI membranes. ASME conference on fuel cell science, engineering and technology, Irvine, CA, 2006.
[13] Liu Z, Wainright J, Litt MH, Savinell R. Study of the oxygen reduction reaction (ORR) at a Pt interfaced with phosphoric acid doped polybenzimidazole at elevated temperature and low relative humidity. Electrochem Acta 2006;51:3914.
[14] Qingfeng L, Hjuler HA, Bjerrum NJ. Phosphoric acid doped polybenzimidazole membranes: physiochemical characterization and fuel cell applications. J Appl Electrochem 2001;31:773–9.
[15] Bouchet R, Siebert E. Proton conduction in acid doped polybenzimidazole. Solid State Ionics 1999;118:287–99.
[16] Qingfeng L, He R, Berg RW, Hjuler HA, Bjerrum NJ. Water uptake and acid doping of polybenzimidazoles as electrolyte membranes for fuel cells. Solid State Ionics 2004;168:177.
[17] Klinedinst K, Bett JAS, Macdonald J, Stonehart P. Oxygen solubility and diffusivity in hot concentrated H_3PO_4. Electroanal Chem Interfacial Electrochem 1974;57:281.
[18] Bernardi DM, Verbrugge MW. A mathematical model of the solid-polymer-electrolyte fuel cell. J Electrochem Soc 1992;139:2477–91.
[19] Boedeker Plastics Inc. Celazole® polybenzimidazole specifications. Retrieved 15 June 2005, from ⟨http://www.boedeker.com/celazo_p.htm⟩.
[20] University of California, San Diego (UCSD). Properties for graphite. Retrieved 15 June 2005, from ⟨http://casl.ucsd.edu/data_analysis/carpet_plots.htm⟩.
[21] Wark K, Wark Jr. K. Advanced thermodynamics for engineers. New York: McGraw-Hill; 1994.
[22] Welty JR, Wicks CE, Wilson RE. Fundamentals of momentum, heat and mass transfer. New York: Wiley; 1969.